Hindawi
Adsorption Science & Technology
Volume 2021, Article ID 9193052, 12 pages
https://doi.org/10.1155/2021/9193052

Research Article

Characterization of Co^{2+}- and Fe^{3+}-Codoped TiO_2 Nanomaterials for Photocatalytic Degradation of Organic Pollutants under Visible Light Irradiation

Nguyen Thi Tuyet Mai,[1] Nguyen Kim Nga,[1] Dang Thi Minh Hue,[1] Ta Ngoc Dung,[1] Huynh Dang Chinh,[1] and Tran Quang Huy[2]

[1]*School of Chemical Engineering, Hanoi University of Science and Technology, 1 Dai Co Viet Road, Hanoi, Vietnam*
[2]*Phenikaa University Nano Institute (PHENA), Phenikaa University, Hanoi 12116, Vietnam*

Correspondence should be addressed to Nguyen Kim Nga; nga.nguyenkim@hust.edu.vn

Received 1 August 2021; Revised 4 October 2021; Accepted 11 October 2021; Published 18 November 2021

Academic Editor: Tien Duc Pham

In this study, TiO_2 nanomaterials were prepared using a solvothermal method and codoped with Co^{2+} and Fe^{3+} ions for the photocatalytic degradation of organic pollutants under visible light. The physicochemical properties of the obtained materials were studied by powder X-ray diffraction, field emission electron scanning microscopy, energy-dispersive X-ray spectroscopy, and nitrogen adsorption isotherms. Optical absorption was characterized by UV-vis absorption spectroscopy. The photocatalytic activities of the prepared materials were evaluated through methylene blue (MB) degradation under visible light irradiation. Results showed the excellent performance of MB degradation investigated on TiO_2 samples codoped with Co^{2+} and Fe^{3+} in comparison with undoped and Co^{2+}-doped TiO_2 samples. The codoped TiO_2 samples degraded 85%–90% of MB after 120 min, whereas all the prepared TiO_2 samples were composed of pure anatase phase and had a spherical-like shape and mean crystalline size ranging from 6.2 nm to 7.8 determined by Scherrer's equation. The optical absorption of the TiO_2 codoped with Co^{2+} and Fe^{3+} was significantly enhanced toward the visible light region. The pseudo-second-order kinetic model fits well for the degradation of MB on as-prepared TiO_2 codoped with Co^{2+} and Fe^{3+}.

1. Introduction

The development of metal oxide nanoparticles has been extensively attracted as adsorbents and photocatalysts for the treatment of dye-containing wastewater [1–3]. Titanium dioxide (TiO_2) nanoparticles have considerable attention because of their long-term stability, low cost, and nontoxicity [4]. However, the major drawback of TiO_2 is a large bandgap energy (~3.2 eV and 3.0 eV for anatase and rutile phases, respectively), and it requires ultraviolet (UV) irradiation (wavelength, $\lambda < 387$ nm) for activation. Many attempts have been conducted to extend the photocatalytic activity of TiO_2 from a UV to visible light region (wavelength, λ: 400-700 nm). Doping of TiO_2 with transition metals or nonmetals is the most promising approach used to activate it due to the bandgap energy reduction [5]. Transition metals can provide additional energy levels within the bandgap of a TiO_2 photocatalyst. Electron transfer from one of these levels to the conduction band requires lower photon energy than those of undoped TiO_2 [6]. Various transition metal ions have been studied to dope with TiO_2, including Co [7], Fe [8], Cr [9], Ni [10], and V [11], etc. Furthermore, many researchers have also focused on codoping of TiO_2 with two or more metal ions for enhancement of photocatalytic degradation of organic pollutants under solar light irradiation such as Mn and Co [12]; Ni and Cr [13]; Fe, Co, and S [14]; and Fe and Pr [15]. It indicated that codoped TiO_2 could expand its light absorption range toward visible light and thus enhance its photocatalytic efficiency, which is higher than that of single-doped TiO_2. It was reported that Mn^{2+}- and Co^{2+}-codoped TiO_2 could degrade about 97% of enoxacin, which was higher than that of Co^{2+} single-

doped TiO_2 (degradation percentage ~48%) after 80 min of exposure to solar light [12]. A recent work also demonstrated that Ni/Cr-codoped TiO_2 exhibited a higher efficiency of 95.6% for MB degradation after 90 min under sunlight, compared to Ni-doped TiO_2 (Ni-doped TiO_2 degraded ~28%-59% of MB depending on the amount of Ni doping) [13]. The photocatalytic degradation of Acid Orange 7 azo dye under visible light using Fe^{3+}- and Pr^{3+}-codoped TiO_2 was much more enhanced compared to undoped TiO_2 and Fe^{3+}single-doped TiO_2 [15]. Those studies indicated that the photocatalytic activity of doped TiO_2 material is greatly dependent on the nature of the dopant ions and their doping concentration and preparation, in which optimal conditions for the synthesis decide the ability of nanomaterials applied for the photodegradation of organic pollutants in wastewater. Fe^{3+} has been considered the best dopant among the transition metals used for increasing the photocatalytic activity of TiO_2 thanks to its similar radius to Ti^{4+} (0.63 Å and 0.60 Å, respectively). TiO_2 doping with Co^{2+} showed excellent degradation activity of dye molecules; however, the optimal concentration of Co^{2+} is needed to enhance activity, because the high percentage of Co^{2+} leads to a reduction in the photocatalytic activity [14].

In this study, we aimed to synthesize and characterize TiO_2 nanoparticles codoped with Co^{2+} and Fe^{3+} ions using the solvothermal method. The effect of the doping concentration of Co^{2+} was investigated to determine the optimal condition for preparing a photocatalyst with high activity in the visible light region. The obtained nanomaterials were investigated by various physicochemical methods, including XRD, FE-SEM, EDXS, nitrogen adsorption-desorption isotherms, and UV-vis absorption. Photocatalytic activities of prepared nanomaterials were evaluated for degradation of methylene blue (MB). Our results indicated that the prepared TiO_2 materials codoped with Co^{2+} and Fe^{3+} showed a highly photocatalytic efficiency compared to single-doped TiO_2. This nanomaterial could be an effective alternative for the treatment of wastewater in the textile industry.

2. Materials and Methods

2.1. Chemicals and Preparation. All chemicals were of analytical grade and used as received without further purification. Tetraisopropyl orthotitanate ($Ti(i\text{-}OC_3H_7)_4$), acetylacetone ($C_5H_8O_2$), ethanol (C_2H_5OH), and methylene blue $C_{16}H_{18}ClN_3S$ (MB) were obtained from Merck. Cobalt (II) acetate tetrahydrate ($(CH_3COO)_2Co{\cdot}4H_2O$) and iron (III) nitrate nonahydrate ($Fe(NO_3)_3{\cdot}9H_2O$) were purchased from China. Double-distilled water was used for preparing all solutions.

Single doping of TiO_2 with Co^{2+} and codoping with Co^{2+} and Fe^{3+} were conducted by the solvothermal synthesis. The obtained samples were referred to as TiO_2-*x*%Co-*y*%Fe, with *x* and *y* showing the molar Co/Ti and Fe/Ti ratio in the starting materials, respectively. In a typical experiment, a mixture consisting of 14.5 mL of C_2H_5OH and 0.5 mL of $C_5H_8O_2$ was stirred for 15 min. The mixture was slowly added with 2.96 mL of $Ti(i\text{-}OC_3H_7)_4$ as a precursor and stirred for another 30 min (mixture 1). Desired amounts of $(CH_3COO)_2Co{\cdot}4H_2O$ and $Fe(NO_3)_3{\cdot}9H_2O$ were dissolved in another mixture consisting of 5 mL of C_2H_5OH, 1 mL of $C_5H_8O_2$, and 0.18 mL of H_2O for 30 min. The mixed solution was then dropped into mixture 1 with continuous stirring for 30 min and then transferred to a 100 mL Teflon-lined stainless-steel autoclave maintained at 180°C for 12 h. The product was washed several times with double-distilled water until pH 7, dried at 100°C for 24 h, and ground on agate mortar. Single-doped and codoped TiO_2 samples were designated as TiO_2-1%Co, TiO_2-2.5%Co, TiO_2-5%Co, TiO_2-1%Co-2.5%Fe, and TiO_2-2.5%Co-2.5%Fe. TiO_2 nanoparticles were also prepared as a control and denoted as undoped TiO_2.

2.2. Material Characterization. X-ray diffraction (XRD) patterns of the prepared TiO_2 samples were recorded with a D8 ADVANCE Bruker Diffractometer within 2θ range of 20°–80° with a scan step of $0.03^\circ{\cdot}s^{-1}$ under Cu-Kα radiation ($\lambda = 0.1.54056$ nm). The surface morphology of the TiO_2 samples and representative doped TiO_2 samples was observed by field emission scanning electron microscopy (FE-SEM, Hitachi S-4800, Japan). The average nanoparticle sizes were calculated from the scanning electron microscopic (SEM) images by using ImageJ software. The elemental composition of the samples was analyzed through energy-dispersive X-ray spectroscopy (EDXS, Nova NanoSEM 450, FEI). The nitrogen adsorption-desorption isotherms of the representative TiO_2 samples were measured at -196°C with a Micromeritics ASAP 2020 apparatus. The total surface areas of the samples were determined by the Brunauer–Emmett–Teller (BET) method, and the pore size distribution was determined through the Barrett–Joyner–Halenda (BJH) method using desorption curves. UV-vis absorption spectra were recorded on the Jasco V-670 spectrometer.

The photocatalytic activity of the prepared TiO_2 samples was evaluated by degradation of MB under visible light irradiation. A 250 W Osram mercury lamp equipped with a UV cut-off filter was used as a visible light source. In a typical experiment, 40 mg of the prepared TiO_2 sample was added into a 100 mL quartz photoreactor containing 50 mL of $14\ mg{\cdot}L^{-1}$ MB solution. The reaction mixture was then stirred in the dark at a constant speed of 150 rpm for 30 min to reach the adsorption-desorption equilibrium. The resulting mixture was irradiated under the visible light source for up to 120 min. After predefined intervals (30, 60, 90, and 120 min), the samples were removed from the photoreactor and centrifuged. The residual concentration in the supernatant was measured with a UV-vis spectrometer (Agilent 8453, USA) at a wavelength of 665 nm. MB concentration was determined using a linear regression equation obtained by plotting a calibration curve of MB within a range of known concentrations. The photocatalytic ability of the TiO_2 samples was evaluated through the percentage of MB degradation as follows:

$$\text{Degradation percent} = \frac{C_o - C}{C_o} \cdot 100\%, \quad (1)$$

where C_o is the initial concentration of MB and C is the remaining concentration of MB at a specific time of measurement.

3. Results and Discussion

3.1. Characterization of the Synthesized Materials. The XRD patterns of the synthesized samples (undoped, single-doped, and codoped TiO_2) are shown in Figure 1. The results demonstrated the formation of monocrystalline TiO_2 in the anatase phase in all samples. The XRD pattern of undoped TiO_2 samples (Figure 1(a)) shows typically crystalline peaks at $2\theta = 25.1^\circ$, 37.67°, 47.71°, and 54.11° corresponding to crystal planes (101), (111), (200), and (211), respectively, which can be indexed to the anatase phase of TiO_2 (JCPDS card no. 21-1272). For single-doped and codoped TiO_2 samples, those diffraction peaks are observed at $2\theta = 25.22^\circ$, 25.25°, 25.30°, 25.34°, and 25.37°; 37.85°, 37.90°, 38°, 38.09°, and 38.12°; 47.82°, 47.88°, 47.92°, 47.99°, and 48.11°; and 54.35°, 54.41°, 54.44°, 54.46°, and 54.51° (see Figures 1(b)–1(f)) for TiO_2-1%Co, TiO_2-2.5%Co, TiO_2-5%Co, TiO_2-1%Co-2.5%Fe, and TiO_2-2.5%Co-2.5%Fe, respectively. The data indicated that the typical peaks of the anatase TiO_2 in single-doped and codoped TiO_2 samples were slightly shifted to higher values than those of undoped TiO_2 samples. The codoped TiO_2 samples (Figures 1(e) and 1(f)) exhibited a decrease in peak intensity and slight broadening of the peaks compared with those of undoped TiO_2 and single-doped TiO_2 samples (Figures 1(a)–1(d)). Moreover, no characteristic peaks attributed to cobalt and iron compounds were detected in the XRD patterns, which can be attributed to the very low dopant amount in the samples. The observations suggested that Co^{2+} and Fe^{3+} cations were successfully introduced into the lattice of TiO_2. The average particle sizes of the samples were calculated from the full width at half maximum (FWHM) of the (101) diffraction peak according to the Debye–Scherrer equation [16]:

$$D = \frac{0.9\lambda}{\beta \cos\theta} \quad (2)$$

where λ is the X-ray wavelength (0.15406 nm), β is the line width at half maxima of peaks, and θ represents the Bragg angle of X-ray diffraction. The obtained results (Table 1) showed that the average particle sizes of all samples were at a nanosized scale ranging from 6.2 nm to 7.8 nm. The single-doped and codoped TiO_2 samples had a smaller size than the undoped TiO_2 samples. The undoped TiO_2 samples had the largest mean particle size of 7.8 nm. Among the three Co-doped TiO_2 samples, TiO_2-1%Co samples had the smallest particle size with a mean particle size of 6.8 nm. The average particle size of Co-doped TiO_2 samples increased from 6.8 nm to 7.5 nm with an increasing Co/Ti molar ratio from 1% to 5% in the samples. The high doping amount of Co resulted in an increase in the particle size, which was attributed to the larger radius of Co^{2+} (0.74 Å) than that of Ti^{4+} (0.60 Å). Therefore, the Co/Ti molar ratio of 1% was considered to be optimal. This ratio was further used to prepare TiO_2 codoped with Co and Fe with varying

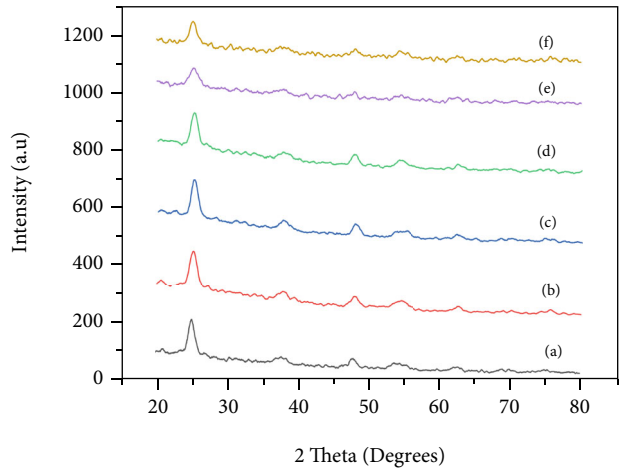

Figure 1: XRD patterns of (a) undoped TiO_2, (b) TiO_2-1%Co, (c) TiO_2-2.5%Co, (d) TiO_2-5%Co, and co-doped TiO_2: (e) TiO_2-1%Co-2.5%Fe and (f) TiO_2-2.5%Co-2.5%Fe.

Co/Ti molar ratios from 1% to 2.5% and a fixed Fe/Ti molar ratio of 2.5%. Previous studies [14, 15] reported that the Fe-doped TiO_2 can extend more excellent absorption in the longer wavelength range than TiO_2. As a result, we chose iron as a codopant element with cobalt for extending the light absorption of TiO_2 nanoparticles toward the visible region. The Fe/Ti molar ratio of 2.5% was used in the synthesis of codoped TiO_2 samples, because the higher Fe content may lead to the formation of iron oxide during thermal treatment at 180°C, decrease the synthesis yield, and/or distort the lattice of TiO_2. As shown in Table 1, TiO_2-1%Co-2.5%Fe samples had smaller sizes (their mean particle sizes are 6.2 nm) than TiO_2-2.5%Co-2.5%Fe samples (their mean particle sizes are 7.6 nm). These results demonstrated that TiO_2 codoped with Co and Fe inhibited the crystal growth of the particles and effectively decreased the particle size; the high doping amount of Co also resulted in an increase in the particle size of the codoped TiO_2 samples.

The morphology of the synthesized TiO_2 samples was further observed through FE-SEM imaging. Figure 2 presents the FE-SEM images of the representative samples: undoped TiO_2 (Figures 2(a) and 2(b)), TiO_2-1%Co (Figures 2(c) and 2(d)), TiO_2-5%Co (Figures 2(e) and 2(f)), and TiO_2-1%Co-2.5%Fe (Figures 2(g) and 2(h)) at magnifications of 100 k and 200 k. The results indicated that the synthesized TiO_2 samples consisted of numerous crystalline particles that agglomerated to form tiny clusters. The FE-SEM images demonstrated that the particles were spherical and had uniform size distribution. The calculations from the FE-SEM images confirmed that the average sizes were 26.5, 23.8, 27, and 20.8 nm for undoped TiO_2, TiO_2-1%Co, TiO_2-5%Co, and TiO_2-1%Co-2.5%Fe samples, respectively. These results showed deviations from the data obtained from XRD due to the agglomeration of the nanoparticles in the FE-SEM images. However, the results were in agreement with the XRD results, confirming that Co and Fe doping can suppress TiO_2 particle growth and the TiO_2-1%Co-2.5%Fe sample had the smallest particle size with a narrow distribution of the particle size (inset in Figure 2).

Table 1: Mean crystalline size and phase of the prepared TiO_2 samples.

Samples	Undoped TiO_2	TiO_2-1%Co	TiO_2-2.5%Co	TiO_2-5%Co	TiO_2-1%Co-2.5%Fe	TiO_2-2.5%Co-2.5%Fe
Crystalline phase	Anatase	Anatase	Anatase	Anatase	Anatase	Anatase
Mean crystalline size	7.8 nm	6.8 nm	7.4 nm	7.5 nm	6.2 nm	7.6 nm

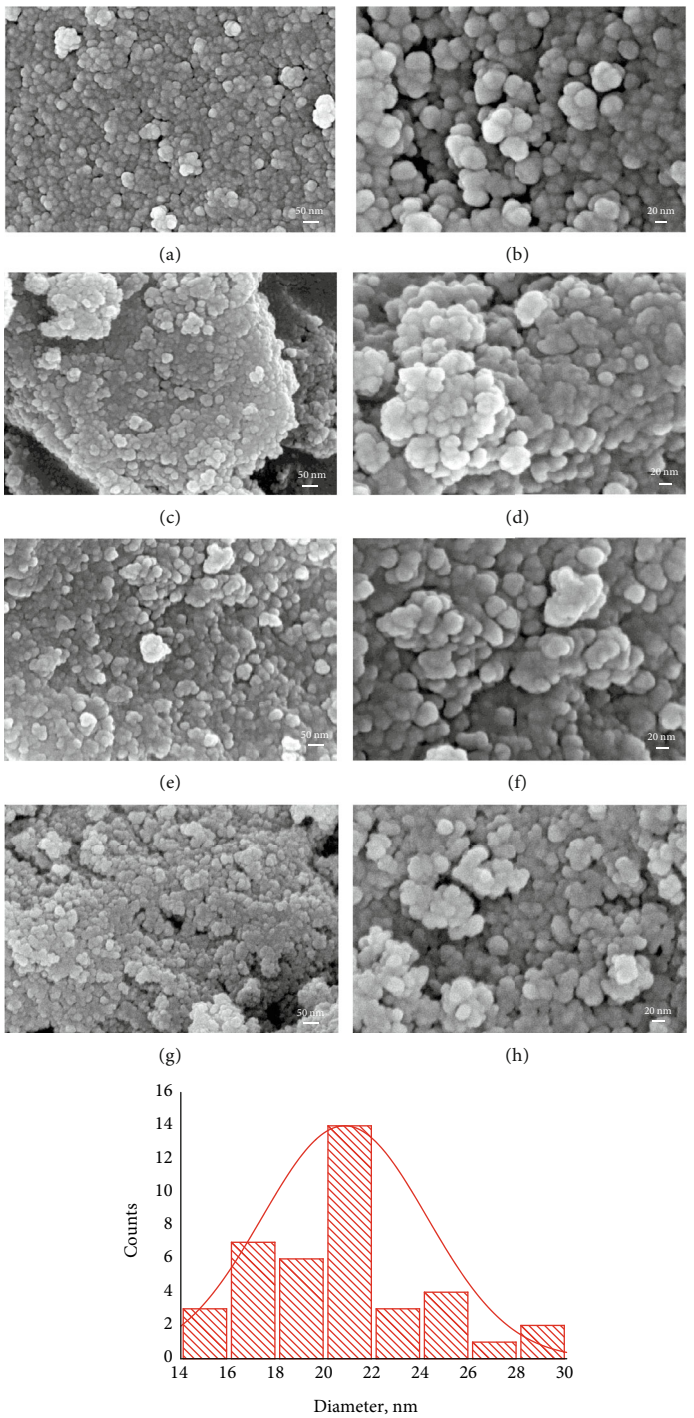

Figure 2: FE-SEM images of undoped TiO_2 (a, b), TiO_2-1%Co (c, d), TiO_2-5%Co (e, f), and TiO_2-1%Co-2.5%Fe (g, h) samples with magnifications of 100 k and 200 k. Inset shows a particle size distribution of TiO_2-1%Co-2.5%Fe samples.

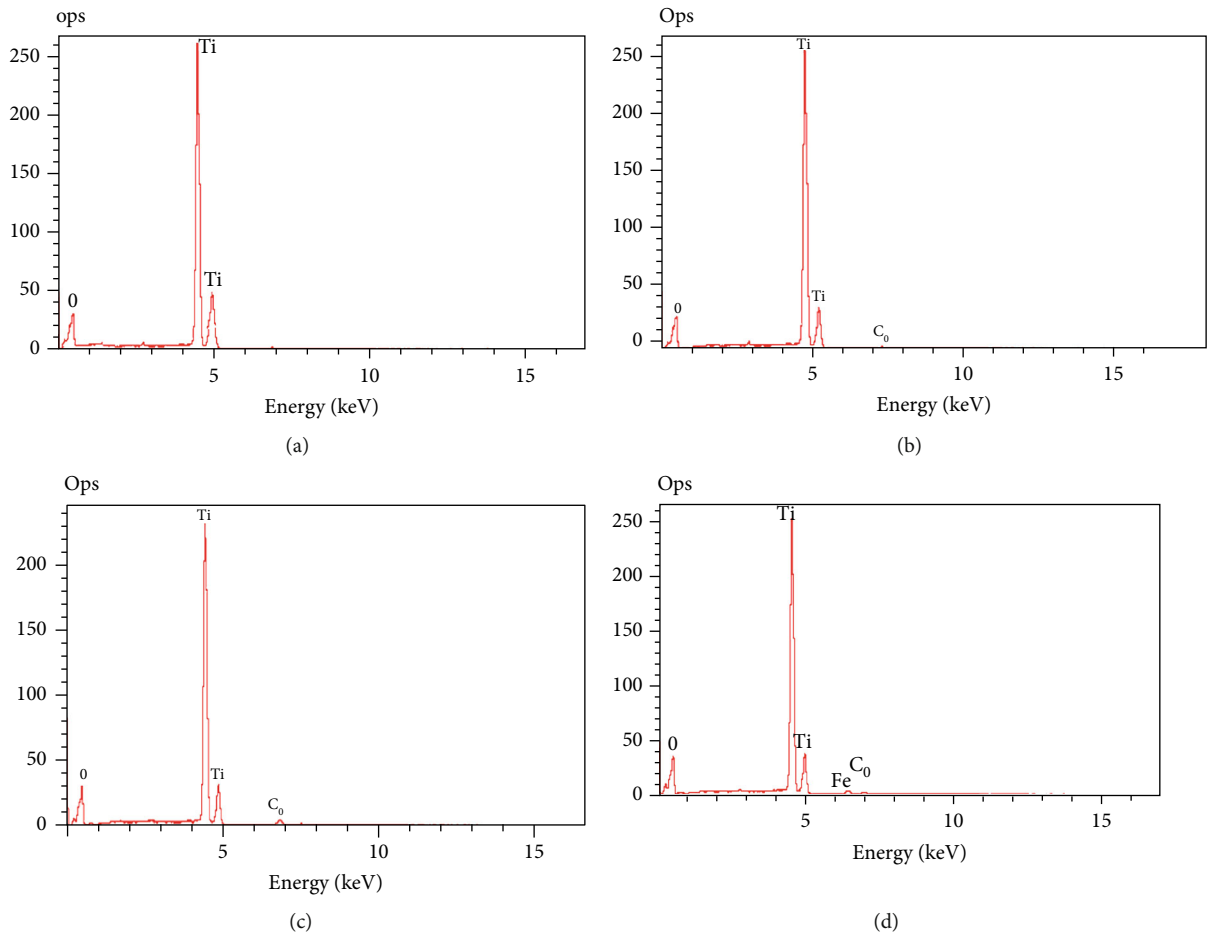

FIGURE 3: EDXS spectra of (a) undoped TiO_2, (b) TiO_2-1%Co, (c) TiO_2-5%Co, and (d) TiO_2-1%Co-2.5%Fe samples.

The presence of doping metals on the TiO_2 samples was determined through EDXS analyses. The EDXS spectra of the representative TiO_2 samples (undoped TiO_2, TiO_2-1%Co, TiO_2-5%Co, and TiO_2-1%Co-2.5%Fe) are presented in Figure 3. As shown in Figures 3(a), O and Ti were found to be the major components of undoped TiO_2 with 65.35 at% and 33.65 at%, respectively. Co was detected as the doping component of TiO_2-1%Co and TiO_2-5%Co samples because tiny peaks were observed in the EDXS spectra (Figures 3(b) and 3(c)), which were attributed to the presence of Co in the samples (0.21 at% and 0.89 at%, respectively). The contents of Co and Fe in TiO_2-1%Co-2.5%Fe samples were 0.28 at% and 0.74 at%, respectively (Figure 3(d)). The results confirmed that Co and Fe were successfully doped in the TiO_2 samples.

Nitrogen adsorption-desorption isotherms were determined for the representative samples to analyze and quantify the pore structure and surface area of doped and codoped TiO_2 samples. Figure 4 presents the nitrogen adsorption-desorption isotherms of three selected samples: TiO_2-1%Co (Figure 4(a)), TiO_2-5%Co (Figure 4(b)), and TiO_2-1%Co-2.5%Fe (Figure 4(c)). Results in Figure 4 indicate that the three samples had a similar hysteresis loop, which could be associated with capillary condensation in mesopores. The hysteresis loops of these samples, which were observed in the P/P_o range of 0.42–0.82, were characterized by a type IV isotherm with an H_2 hysteresis loop [17]. The results suggested that the TiO_2 samples contained ink-bottle pores, leading to pore blocking/percolation effects during desorption in mesopore networks. Pore size distribution was calculated by the BJH method using data on the desorption curves (Figure 5). The surface areas of the synthesized TiO_2 samples were determined by using the BET method. The surface characteristics of these samples are summarized in Table 2 and compared with those of undoped TiO_2. TiO_2-1%Co and TiO_2-1%Co-2.5%Fe samples showed a narrow pore size distribution (Figures 5(a) and 5(c)) with average mesopore diameters of 3.97 and 4.1 nm, respectively (Table 2). TiO_2-5%Co samples exhibited a wider pore size distribution that scattered from 2.5 nm to 6.5 nm and mainly concentrated at 5.1 nm (Figure 5(b) and Table 2). Undoped TiO_2 showed a larger mean pore size of 6.7 nm than the doped and codoped TiO_2. As shown in Table 2, the prepared TiO_2 samples did not have significant discrepancies in their BET surface area. Relatively high BET surface areas were determined as follows: 170 m^2/g for TiO_2-1%Co, 164 m^2/g for TiO_2-5%Co, and 174 m^2/g for TiO_2-1%Co-2.5%Fe, which are slightly higher than that of undoped TiO_2 (160 m^2/g). The large BET surface areas of the doped and codoped TiO_2 samples confirmed the better adsorption ability of the frameworks of TiO_2. This finding may be due to the linkage between the dopant ions (Co^{2+} and Fe^{3+}) and titanium by an

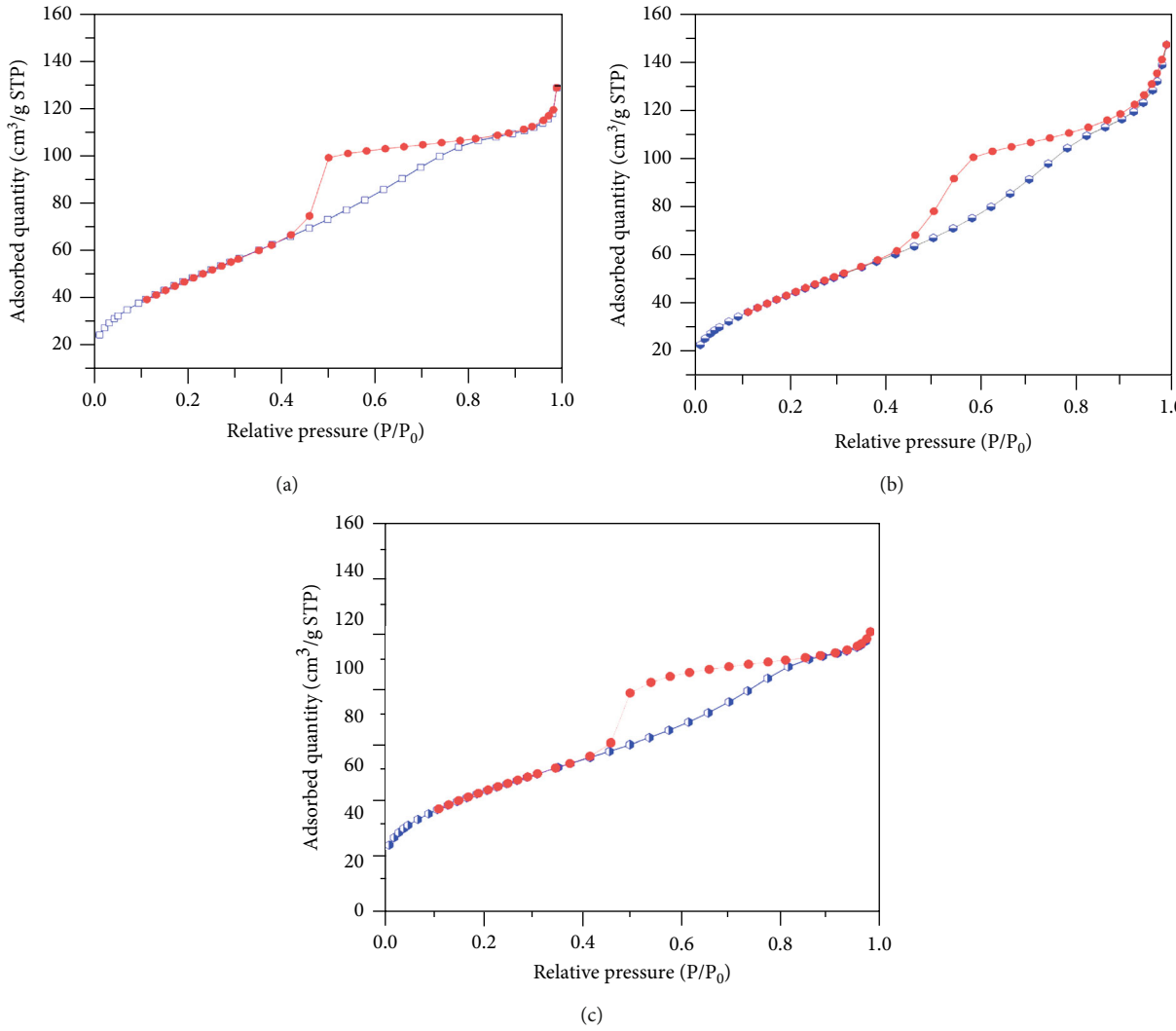

FIGURE 4: Nitrogen adsorption-desorption isotherms of representative samples: (a) TiO_2-1%Co, (b) TiO_2-5%Co, and (c) TiO_2-1%Co-2.5%Fe samples.

oxygen bridge, which effectively increased their specific surface areas.

Table 3 compares the BET surface areas of doped and codoped TiO_2 materials of the present work with those of other doped and codoped TiO_2 materials reported previously. The BET surface areas of doped and codoped TiO_2 materials of our work were within 164–174 m^2/g, which were higher than those of Fe-doped TiO_2 materials [18, 19], Co-doped TiO_2 materials [20], Cr- and Fe-doped TiO_2 materials [18], and Fe- and La-doped TiO_2 materials [19] (Table 3). The larger BET surface areas of the doped and codoped TiO_2 materials of the present work were possibly due to their smaller particle sizes ranging from 6.2 nm to 7.5 nm (Table 3), depending on the doping amount. The doped TiO_2 materials of our work were prepared under more favorable conditions (solvothermal treatment at 180°C without calcination). The other TiO_2 materials were prepared by hydrothermal treatment or sol-gel method, followed by calcination, which resulted in the formation of larger particle sizes and significant loss of the BET surface area (Table 3).

The UV-vis absorption spectra of undoped TiO_2, doped TiO_2, and codoped TiO_2 samples were recorded to study their optical properties (Figure 6). As shown in Figure 6 (curve a), the undoped TiO_2 sample was characterized by a narrow absorption spectrum, ranging from 250 nm to 370 nm in the UV region. No visible light absorption was observed for the undoped TiO_2 sample. Co-doped TiO_2 (Figure 6, curves b–d) and Co- and Fe-doped TiO_2 samples (Figure 6, curves e and f) had broader absorption spectra, which shifted toward longer wavelengths in the visible light region. The absorption spectra of Co-doped TiO_2 samples had maximum peaks at about 330–340 nm, but the shoulder of the peaks shifted to the visible range (400-700 nm). TiO_2 samples codoped with Co and Fe were characterized by a broader maximum peak at 400–500nm and stronger intensity of the absorption shoulder in the visible region compared with those of single-doped TiO_2 samples. Figure 6 shows that the absorption edges of TiO_2 codoped with Co and Fe moved remarkably, with a redshift to the visible region in comparison with undoped TiO_2. These optical

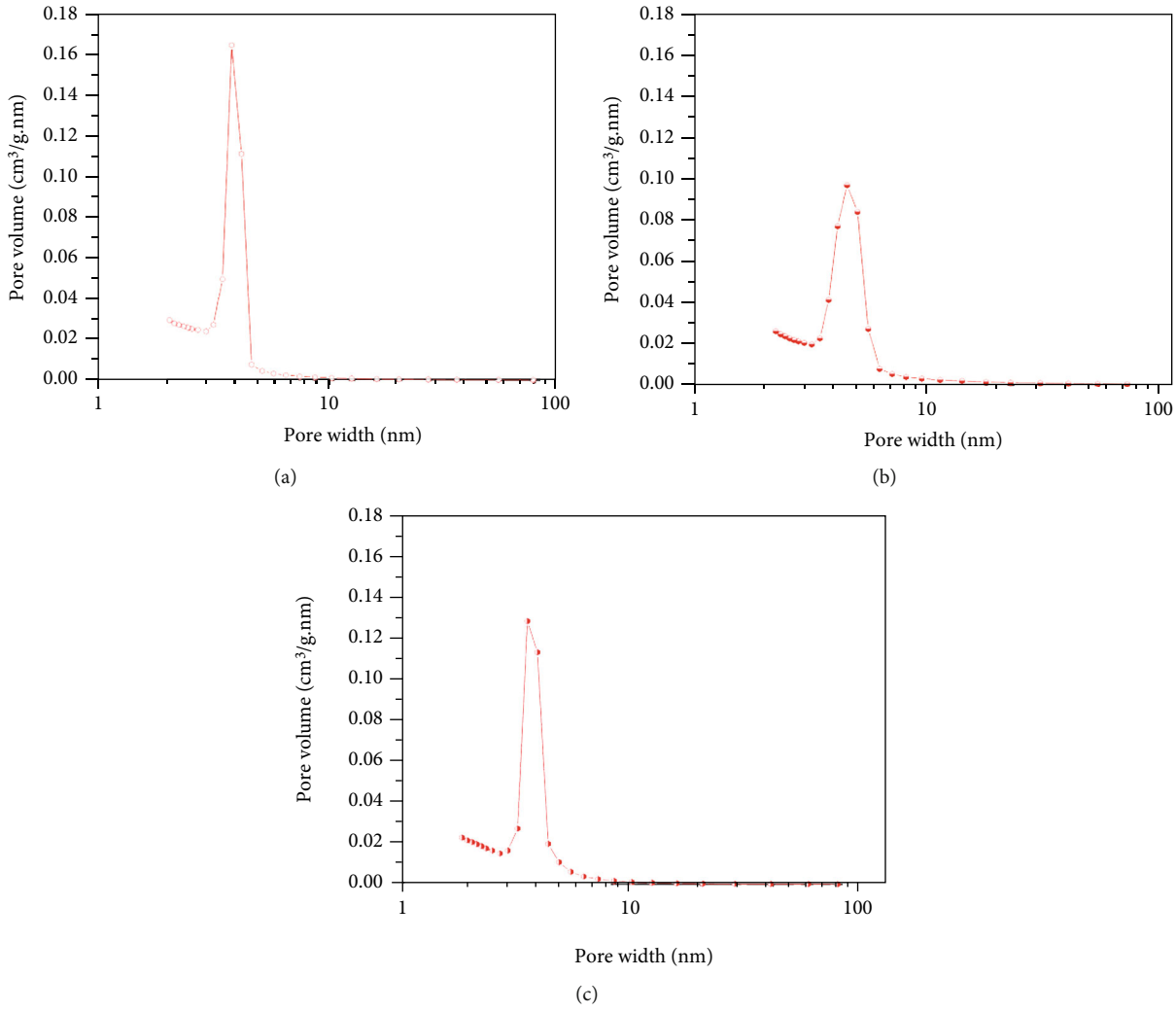

Figure 5: Pore size distributions of representative samples: (a) TiO_2-1%Co, (b) TiO_2-5%Co, and (c) TiO_2-1%Co-2.5%Fe samples.

Table 2: Surface characteristics of the representative TiO_2 samples.

Samples	S_{BET} [a] (m^2/g)	V_{BJH} [b] (cm^3/g)	D_p [c] (nm)
TiO_2-1%Co	170	0.18	3.97
TiO_2-5%Co	164	0.23	5.1
TiO_2-1%Co-2.5%Fe	174	0.16	4.1
Undoped TiO_2	160	0.29	6.7

[a]BET surface area. [b]Total pore volume determined using desorption curves of the isotherms. [c]Peak pore sizes from the pore size distributions.

absorption characteristics of TiO_2 codoped with Co and Fe were possibly due to absorption induced by dopants. The absorption edges can be extrapolated by making a tangent line of the UV-vis absorption spectra [21]. Therefore, the bandgap energies of the prepared TiO_2 samples were estimated from the UV-vis spectra via the following equation:

$$E_g = \frac{1240}{\lambda} \quad (3)$$

The bandgap energy levels of Co-doped TiO_2 samples were estimated to be 2.03 eV, 2.00 eV, and 1.99 eV (for TiO_2-1%Co, TiO_2-2.5%Co, and TiO_2-5%Co, respectively), which were higher than those of Co- and Fe-codoped TiO_2 samples (their bandgap energies are 1.65 eV and 1.59 eV for TiO_2-1%Co-2.5%Fe and TiO_2-2.5%Co-2.5%Fe, respectively). The calculated bandgap energies of single-doped and codoped TiO_2 samples were lower than that of undoped TiO_2 samples (~3.25 eV). The results revealed that the dopant elements were successfully incorporated into the TiO_2 crystal lattice and extended the optical absorption toward the visible light region. TiO_2 samples codoped with Co and Fe had stronger optical absorption of the visible light than single-doped and undoped TiO_2 samples. This means that the TiO_2 codoped with Co and Fe can absorb visible light in a much wider range of wavelengths than undoped TiO_2 and single-doped TiO_2 samples, which is beneficial for increasing the photocatalytic efficiency under visible light.

3.2. Photocatalytic Activities of the Prepared TiO_2 Materials for Degradation of MB. Before the photocatalytic reaction, the adsorption for MB removal on the synthesized TiO_2 materials was conducted under dark conditions. Results

Table 3: Comparison of the BET surface areas of the TiO_2 samples prepared in this work with those of previous works.

Materials	Synthetic conditions	S_{BET} (m^2/g)	Particle size (nm)	References
TiO_2-1%Co	Solvothermal treatment at 180°C without calcination	170	6.8	This work
TiO_2-5%Co	Solvothermal treatment at 180°C without calcination	164	7.5	This work
TiO_2-1%Co-2.5%Fe	Solvothermal treatment at 180°C without calcination	174	6.2	This work
TiO_2-Fe	Hydrothermal treatment at 180°C, calcined at 400°C	89	18	[18]
TiO_2-0.2%Fe	Sol-gel, calcined at 500°C	78	12	[19]
TiO_2-0.2%Fe-2%La	Sol-gel, calcined at 500°C	84	10	[19]
TiO2-0.085%Co	Sol-gel, with following heat treatment from 200°C to 900°C for 30 min	39.7	25	[20]
Fe-Cr-codoped TiO_2	Hydrothermal treatment at 180°C, calcined 500°C	93		[18]

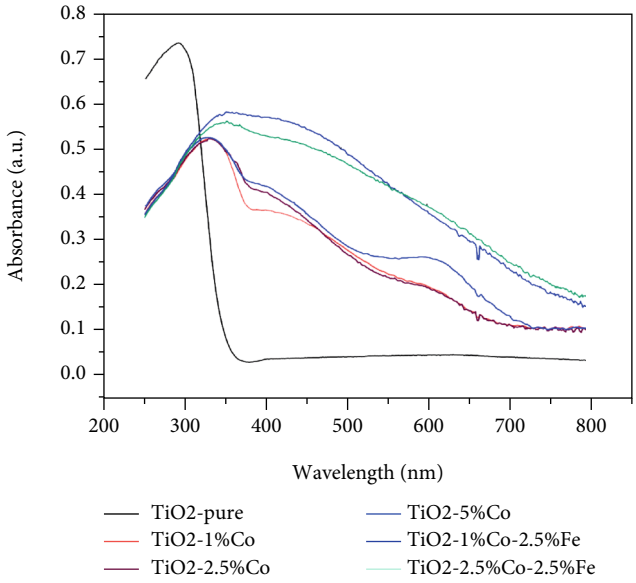

Figure 6: UV-vis spectra of undoped TiO_2, TiO_2-1%Co, TiO_2-2.5%Co, TiO_2-5%Co, TiO_2-1%Co-2.5%Fe, and TiO_2-2.5%Co-2.5%Fe samples.

obtained showed that the percentages of MB removal were only 5%-6% after 60 min for all the synthesized materials, but desorption of MB was observed by prolonging adsorption time for those materials. Therefore, the photocatalytic activities of the prepared TiO_2 samples were evaluated by degrading MB solution under visible light irradiation. The reaction mixture was first stirred in the dark for 30 min to reach the adsorption-desorption equilibrium and to ensure that the degradation of MB obtained is due to the photocatalytic reaction with the presence of the synthesized TiO_2 materials, but not due to the adsorption. Figure 7 shows the percentage of MB degradation over all of the TiO_2 samples (undoped TiO_2, TiO_2-1%Co, TiO_2-2.5%Co, TiO_2-5%Co, TiO_2-1%Co-2.5%Fe, and TiO_2-2.5%Co-2.5%Fe samples) as a function of irradiation time. For comparison, control experiments were performed under the same conditions but without the presence of a photocatalyst (Figure 7, curve MB). As shown in Figure 7 (curve MB), almost no degradation of MB was observed without the photocatalyst (only 7.95% of MB was degraded after 120 min of exposure to visible light irradiation), indicating that MB was unable to self-degrade. Undoped TiO_2 and Co-doped TiO_2 with low doping concentration (TiO_2-1%Co and TiO_2-2.5%Co) showed pure photocatalytic activity. The degradation efficiencies of MB on undoped TiO_2 samples were comparable with those of Co-doped TiO_2 samples with low Co doping concentration for all the tested time points (Figure 7, curves undoped TiO_2, TiO_2-1%Co, and TiO_2-2.5%Co). The degradation percentages of MB were 10.95%, 17.85%, and 17.5% after 120 min of irradiation for undoped TiO_2, TiO_2-1%Co, and TiO_2-2.5%Co, respectively. However, the degradation of MB is enhanced with higher Co doping concentration. The degradation percentages of MB increased three times on TiO_2-5%Co samples and were higher than those on TiO_2-1%Co and TiO_2-2.5%Co samples for all the tested time points. About 39.8% of MB was degraded within 30 min on TiO_2-5%Co and then gradually increased to ~50% by increasing irradiation time up to 120 min. Moreover, the significantly enhanced degradation of MB was observed on codoped TiO_2 samples (Figure 7, curves TiO_2-1%Co-2.5%Fe and TiO_2-2.5%Co-2.5%Fe). The highest degradation of MB was obtained by TiO_2 codoped with 1%Co and 2.5%Fe for all the time points tested. The degradation of MB was almost complete on codoped TiO_2 samples for the tested time; 90% and 85% of MB were degraded on TiO_2-1%Co-2.5%Fe and TiO_2-2.5%Co-2.5%Fe after 120 min, respectively.

The results showed that TiO_2 samples codoped with Co and Fe exhibited higher photocatalytic degradation of MB under visible light than the undoped and single-doped TiO_2 samples, which could be attributed to their lower bandgap values compared to those of the undoped and single-doped TiO_2 samples. These observations indicated that codopant ions had a favorable effect on the photocatalytic performance of the prepared TiO_2 materials. These ions can provide additional energy levels within the bandgap of TiO_2. The bandgap of TiO_2 consists of a contribution from the 2p orbitals of O for the valence band and the 3d orbitals of Ti toward the conduction band, which have a large difference in energy, leading to the activation of TiO_2 in the UV light region with extremely high energy. The band structures of codoped TiO_2 materials are mainly affected by the 3d energy states of the transitional metal ions (Co^{2+} and Fe^{3+}). In fact, the UV-vis absorption studies (Figure 6) revealed that the respective absorption bands of codoped TiO_2 samples effectively shifted toward wavelengths longer

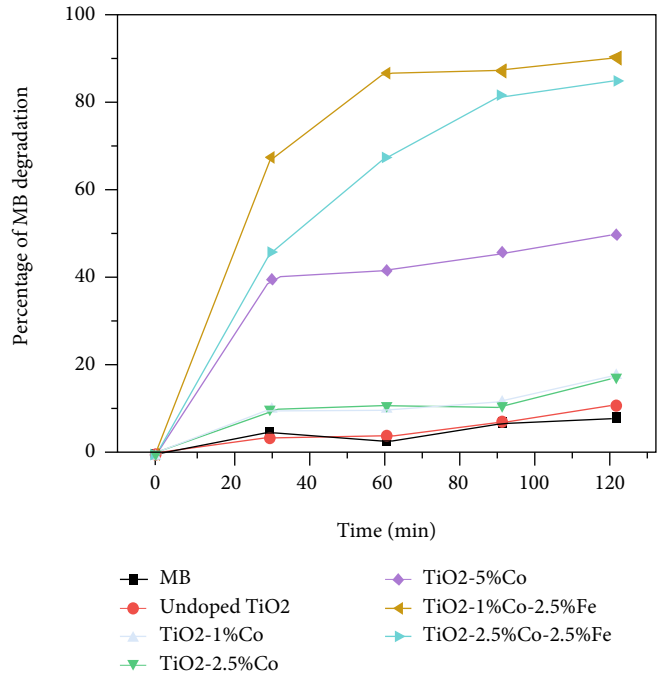

Figure 7: The degradation of MB using different catalysts: undoped TiO_2, TiO_2-1%Co, TiO_2-2.5%Co, TiO_2-5%Co,TiO_2-1%Co-2.5%Fe, and TiO_2-2.5%Co-2.5%Fe samples under visible light irradiation.

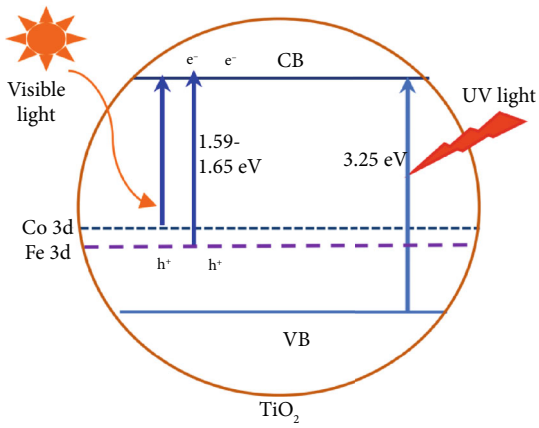

Scheme 1: Band structure of TiO_2 and TiO_2 codoped with Co^{2+} and Fe^{3+}. VB: valence band; CB: conduction band.

than 400 nm. Thus, the partially filled Co/Fe 3d bands were located below the conduction band of TiO_2. Hence, when photons with wavelengths longer than 400 nm are used for illumination, the electrons in the Co 3d and Fe 3d bands, instead of electrons in the valence band of TiO_2, are excited to the conduction band, while Co^{2+} and Fe^{3+} loses one electron and becomes Co^{3+} and Fe^{4+} (see Scheme 1). This phenomenon can induce more photogenerated electrons and holes to participate in the photocatalytic reaction.

As calculated above, the bandgap energy values of codoped TiO_2 samples (1.59 eV-1.65 eV) were lower than those of single-doped TiO_2 samples (1.99-2.03 eV) and undoped TiO_2 (3.25 eV), indicating the lower energy of photons necessary to generate electron transition and holes (h^+) for codoped TiO_2 samples compared to single-doped and undoped TiO_2. These holes can react with water to produce the highly reactive $^{\cdot}OH$, and both holes and $^{\cdot}OH$ have a strong oxidation potential for the degradation of MB.

The plausible reaction mechanism of the photodegradation is given below:

$$TiO_2 + h\nu \longrightarrow e^- + h^+ \quad (4)$$

$$Co^{2+} + h\nu \longrightarrow Co^{3+} + e^- \quad (5)$$

$$Fe^{3+} + h\nu \longrightarrow Fe^{4+} + e^- \quad (6)$$

$$h^+ + H_2O_{ads} \longrightarrow \cdot OH + H^+ \quad (7)$$

$$e^- + O_{2ads} \longrightarrow O_2\cdot^- \quad (8)$$

$$MB + \cdot OH/O_2\cdot^- \longrightarrow \text{degradation products} \quad (9)$$

It is suggested that the photodegradation of MB can be divided into three main steps: (1) the initial step is the formation of electrons (e^-) in the CB and holes (h^+) in the VB upon a light incident on the photocatalyst surface (see equations (4), (5), (6)); (2) the intermediate step includes the formation of $^{\cdot}OH$ and H^+ through the interaction between the holes and H_2O adsorbed on the photocatalyst surface (equation (7)) and of $O_2^{\cdot-}$ due to the reduction of the adsorbed O_2 molecule (equation (8)) that has strong oxidation power, which in turn promotes the decomposition of MB; and (3) the final step is the degradation of MB by $^{\cdot}OH/O_2^{\cdot-}$ radicals.

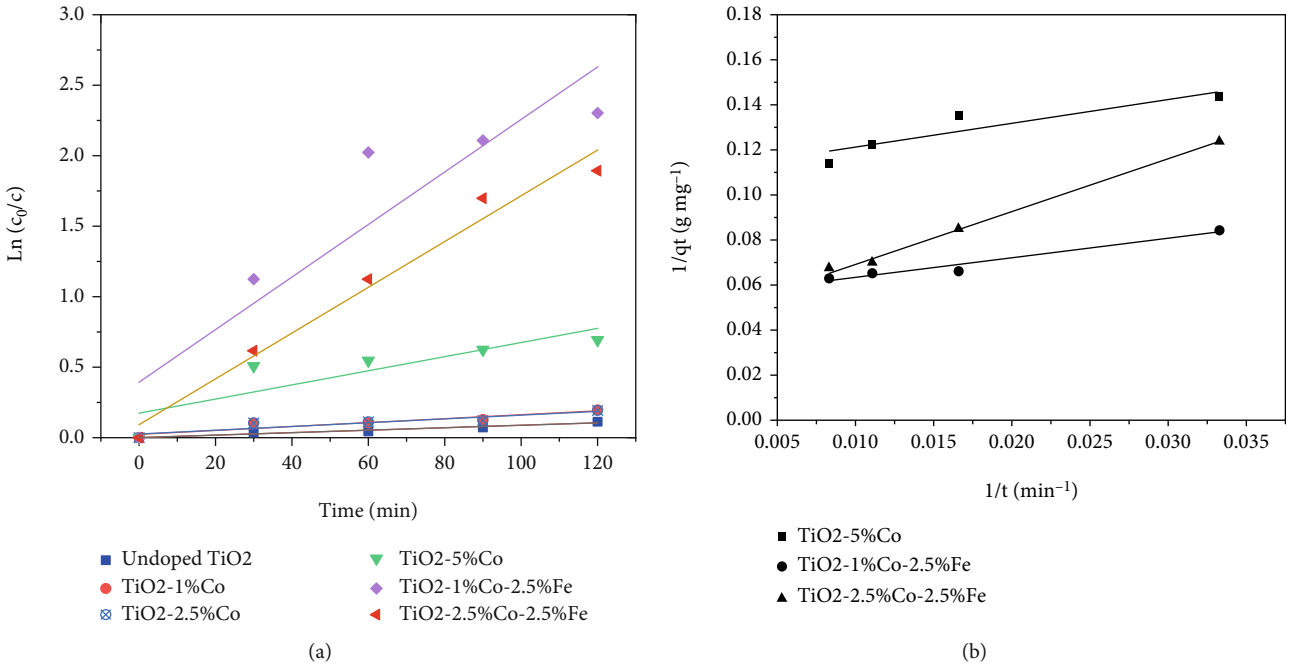

Figure 8: Plots of (a) first- and (b) second-order reaction rates for the degradation of MB over as-prepared TiO_2 materials.

Thus, this work proposed a study to understand the role of Co and Fe in codoped TiO_2 nanoparticles in yielding better performance as a visible light-driven photocatalyst.

The kinetics of photodegradation of MB on as-prepared TiO_2 materials was further investigated using the pseudo-first-order kinetic model [22] as follows:

$$\ln \frac{C_o}{C} = k_1 t, \tag{10}$$

where C_o is the initial concentration of MB, C is the concentration of MB at time t, and k_1 is the apparent reaction rate constant. According to equation (10), a linear regression plot of $\ln (C_o/C)$ vs. time t gives the value of k_1. The experimental data were analyzed using the pseudo-first-order equation; the resulting plots of $\ln (C_o/C)$ vs. time t are shown in Figure 8(a). From the obtained plots in Figure 8(a), the rate constants were found to be $0.0009\,min^{-1}$, $0.0014\,min^{-1}$, $0.0013\,min^{-1}$, $0.005\,min^{-1}$, $0.0186\,min^{-1}$, and $0.0162\,min^{-1}$ with correlation coefficients (R^2) of 0.96, 0.91, 0.90, 0.78, 0.85, and 0.98 for the undoped TiO_2, TiO_2-1%Co, TiO_2-2.5%Co, TiO_2-5%Co, TiO_2-1%Co-2.5%Fe, and TiO_2-2.5%Co-2.5%Fe, respectively. The experimental degradation data of all the TiO_2 samples were also analyzed using the pseudo-second-order kinetic equation proposed by Blanchard et al. [23]:

$$\frac{1}{q_t} = \frac{1}{t}\frac{1}{k_2 q_e^2} + \frac{1}{q_e}, \tag{11}$$

where q_t and q_e are the amounts of dye adsorbed at time t and at equilibrium ($mg{\cdot}g^{-1}$) and k_2 is the pseudo-second-order rate constant ($g{\cdot}mg^{-1}{\cdot}min^{-1}$) for the adsorption process. The linear plots of $1/q_t$ vs. time $1/t$ shown in Figure 8(b) give the values of k_2 and q_e. It could be seen that three TiO_2 samples: TiO_2-5%Co, TiO_2-1%Co-2.5%Fe, and TiO_2-2.5%Co-2.5%Fe showed the best fit in the linear plots of $1/q_t$ vs. $1/t$ with higher values of R^2 (0.83, 0.95, and 0.99, respectively) than those of the pseudo-first-order equation (0.78, 0.85, and 0.98). The values of q_e obtained from the linear plots are $9.03\,mg{\cdot}g^{-1}$, $18.28\,mg{\cdot}g^{-1}$, and $21.78\,mg{\cdot}g^{-1}$ for TiO_2-5%Co, TiO_2-1%Co-2.5%Fe, and TiO_2-2.5%Co-2.5%Fe, which were higher than those of the experimental values ($8.75\,mg{\cdot}g^{-1}$, $14.86\,mg{\cdot}g^{-1}$, and $15.75\,mg{\cdot}g^{-1}$ for TiO_2-5%Co, TiO_2-1%Co-2.5%Fe, and TiO_2-2.5%Co-2.5%Fe, respectively), whereas the undoped TiO_2, TiO_2-1%Co, and TiO_2-2.5%Co samples did not follow the pseudo-second-order equation because of smaller values of R^2 (0.82, 0.55, and 0.54) of the plots $1/q_t$ vs. $1/t$ (not shown), compared to those of the pseudo-first-order plots.

The observations revealed that the degradation of MB on the undoped TiO_2 and Co single-doped TiO_2 samples with 1% Co and 2.5% Co doping can be described by the pseudo-first-order equation. Meanwhile, the pseudo-second order fits better compared to the pseudo-first order for describing the degradation of MB on the TiO_2 doped with 5%Co and codoped with Co and Fe, considering that R^2 of the pseudo-second-order equation was greater than that of the first order for those samples. This clearly explains that the enhanced degradation efficiency of MB is attributed to the high surface area of the TiO_2 codoped with Co and Fe and their reduced bandgap energies.

Table 4 compares the degradation of MB on the TiO_2 materials as prepared in this work with those published in previous works [24–28]. It was found that the TiO_2 codoped with 1%Co and 2.5%Fe in this work showed the highest

Table 4: Comparison of MB degradation of the TiO_2-codoped samples of this work with other materials.

Materials	Synthetic conditions	S_{BET} ($m^2 \cdot g^{-1}$)	Degradation percentage of MB	References
Bi_2O_3	Calcination method at 500°C for 6 h	2.9	70% after 4 h under visible light irradiation	[24]
$CaBi_6O_{10}$	Impregnation-calcination method at 650°C for 12 h	2.5	97% after 4 h under visible light irradiation	[24]
CeO_2/V_2O_5	Thermal decomposition at 400°C for 30 min	—	64.2% after 4 h under visible light	[25]
CeO_2/CuO	Thermal decomposition at 400°C for 30 min	—	70.1% after 4 h under visible light	[25]
ZnO/CdO	Thermal decomposition at 350°C for 3 h	—	75% after 4 h under visible light	[26]
g-C_3N_4-CdS	Precipitation method	166.5	90.45% after 3 h under visible light	[27]
F-doped TiO_2	Sol-gel method, calcined at 500°C for 1 h	39.6	90% after 4 h under visible light	[28]
TiO_2-1%Co-2.5%Fe	Solvothermal method at 180°C	174	90% after 2 h under visible light	This work

photocatalytic efficiency with 90% of MB degraded after visible light irradiation of 2 h. The metal oxide (Bi_2O_3) [24] and mixed metal oxides (e.g., CeO_2/V_2O_5 [24], CeO_2/CuO [25], and ZnO/CdO [26]) exhibited much lower degradation efficiency of MB compared with the TiO_2 materials of our work, which degraded about 64.2%-75% of MB for a longer irradiation time of 4 h. The complex metal oxide $CaBi_6O_{10}$ [24] and nanocomposite g-C_3N_4-CdS [27] demonstrated relatively high degradation percentages of MB (~97% and 90.45% for $CaBi_6O_{10}$ and g-C_3N_4-CdS, respectively), which could be comparable with that of the TiO_2 codoped with 1%Co and 2.5%Fe of our work, but these materials require a quite long irradiation time of 4 h (for $CaBi_6O_{10}$) and 3 h (g-C_3N_4-CdS) to obtain the complete degradation of MB under visible light. Moreover, a similar study reported that TiO_2 doped with 10% F [28] also revealed a high degradation percentage of MB (~90%), but after a much longer irradiation time of 4 h, compared to that of the TiO_2 codoped with Co and Fe of our work. The comparison revealed that the photocatalytic efficiency of the materials depends not only on their band structure but also on their surface characteristics. The excellent photocatalytic performance of the TiO_2 codoped with Co and Fe of our work could be attributed to their larger BET surface area compared to those of the other materials. As a result, the TiO_2 codoped with Co and Fe has more active sites and simultaneously can absorb much more visible light and generate more electron-hole pairs, which in turn enhanced the photocatalytic activity and reduced the reaction time as compared to the other materials.

4. Conclusions

In this work, we presented the characterization of TiO_2 nanoparticles codoped with Co^{2+} and Fe^{3+} synthesized through solvothermal treatment at 180°C without further calcination at high temperatures. Undoped TiO_2 and Co single-doped TiO_2 materials were also prepared using the same procedure to compare with codoped TiO_2 in terms of optical absorption and photocatalytic efficiency for MB degradation. The doped and codoped TiO_2 materials of the present work exhibited better adsorption characteristics (e.g., their BET surface areas of 164-174 m^2/g) than doped and codoped TiO_2 materials of previous works; as-prepared codoped TiO_2 materials had significantly enhanced optical adsorption toward the visible light region. Among the TiO_2 samples studied, the codoped TiO_2 materials showed the highest photocatalytic activity for the degradation of MB; they degraded about 90% of MB within 120 min under visible light irradiation. The TiO_2 samples codoped with Co and Fe in this work showed higher photocatalytic efficiency for the degradation of MB than those of metal oxides, mixed metal oxides, and other materials in the previous works. The pseudo-second-order kinetic model fits well for describing the degradation of MB on the TiO_2 codoped with Co and Fe. Hence, this study provides a simple route to synthesize an effective photocatalyst for the degradation of dye compounds under visible light for wastewater treatment.

Data Availability

All the data used to support the findings of this study are included within the article.

Conflicts of Interest

There are no conflicts of interest to declare.

Acknowledgments

This study was funded by the Vietnam National Foundation for Science and Technology Development (NAFOSTED) under grant number 104.03-2019.313.

References

[1] D. Chen, Y. Cheng, N. Zhou et al., "Photocatalytic degradation of organic pollutants using TiO_2-based photocatalysts: a review," *Journal of Cleaner Production*, vol. 268, p. 121725, 2020.

[2] M. Sun, Y. Fang, S. Sun, and Y. Wang, "Surface co-modification of TiO_2 with N doping and Ag loading for enhanced visible-light photoactivity," *RSC Advances*, vol. 6, no. 15, pp. 12272–12279, 2016.

[3] N. T. T. Mai, N. K. Nga, D. T. M. Hue et al., "Effect of calcination temperature on the structure and characteristics of

cuprous oxide (Cu_2O-ONPs)," in *Proceedings of Second Annual Conference on Materials, Machine. Meth. for Sustainable Development (MMMS2020)*, pp. 375–383, 2021.

[4] Q. Sun, K. Li, S. Wu, B. Han, L. Sui, and L. Dong, "Remarkable improvement of TiO2for dye photocatalytic degradation by a facile post-treatment," *New Journal of Chemistry*, vol. 44, no. 5, pp. 1942–1952, 2020.

[5] M. K. Singh and M. S. Mehata, "Enhanced photoinduced catalytic activity of transition metal ions incorporated TiO_2 nanoparticles for degradation of organic dye: absorption and photoluminescence spectroscopy," *Optical Materials*, vol. 109, p. 110309, 2020.

[6] M. A. Rauf, M. A. Meetani, and S. Hisaindee, "An overview on the photocatalytic degradation of azo dyes in the presence of TiO_2 doped with selective transition metals," *Desalination*, vol. 276, no. 1-3, pp. 13–27, 2011.

[7] P. Jiang, W. Xiang, J. Kuang, W. Liu, and W. Cao, "Effect of cobalt doping on the electronic, optical and photocatalytic properties of TiO_2," *Solid State Sciences*, vol. 46, pp. 27–32, 2015.

[8] J.-H. Shen, H.-Y. Chuang, Z.-W. Jiang, X.-Z. Liu, and J.-J. Horng, "Novel quantification of formation trend and reaction efficiency of hydroxyl radicals for investigating photocatalytic mechanism of Fe-doped TiO_2 during UV and visible light-induced degradation of acid orange 7," *Chemosphere*, vol. 251, p. 126380, 2020.

[9] C. Gomez-Polo, S. Larumbe, A. Gila et al., "Improved photocatalytic and antibacterial performance of Cr doped TiO_2 nanoparticles," *Surfaces and Interfaces*, vol. 22, p. 100867, 2021.

[10] A. Barmeh, M. R. Nilforoushan, and S. Otroj, "Wetting and photocatalytic properties of Ni-doped TiO_2 coating on glazed ceramic tiles under visible light," *Thin Solid Films*, vol. 666, pp. 137–142, 2018.

[11] T. Wang, D. Shena, T. Xua, and R. Jiang, "Photocatalytic degradation properties of V-doped TiO_2 to automobile exhaust," *Science of the Total Environment*, vol. 586, pp. 347–354, 2017.

[12] M. Sayed, A. Arooj, N. S. Shah et al., "Narrowing the band gap of TiO_2 by co-doping with Mn^{2+} and Co^{2+} for efficient photocatalytic degradation of enoxacin and its additional peroxidase like activity: a mechanistic approach," *Journal of Molecular Liquids*, vol. 272, pp. 403–412, 2018.

[13] M. Shaban, A. M. Ahmed, N. Shehata, M. A. Betiha, and A. M. Rabie, "Ni-doped and Ni/Cr co-doped TiO_2 nanotubes for enhancement of photocatalytic degradation of methylene blue," *Journal of Colloid and Interface Science*, vol. 555, pp. 31–41, 2019.

[14] M. Imran, Z. Saeed, M. Pervaiz et al., "Enhanced visible light photocatalytic activity of TiO_2 co-doped with Fe, Co, and S for degradation of Cango red," *Spectrochimica Acta Part A: Molecular and Biomolecular Spectroscopy*, vol. 255, p. 119644, 2021.

[15] A. Mancuso, O. Sacco, V. Vaiano et al., "Visible light active Fe-Pr co-doped TiO_2 for water pollutants degradation," *Catalysis Today*, vol. 380, pp. 93–104, 2021.

[16] U. Holzwarth and N. Gibson, "The Scherrer equation versus the 'Debye-Scherrer equation'," *Nature Nanotechnology*, vol. 6, no. 9, p. 534, 2011.

[17] S. J. Gregg and K. S. W. Sing, *Adsorption, Surface Area and Porosity*, Academic Press, London, 2nd edition, 1982.

[18] E. D. Jeong, P. H. Borse, J. S. Jang et al., "Hydrothermal synthesis of Cr and Fe co-doped TiO_2 nanoparticle photocatalyst," *Journal of Ceramic Processing Research*, vol. 9, pp. 250–253, 2008.

[19] Q. Wang, S. Xu, and F. Shen, "Preparation and characterization of TiO_2 photocatalysts co-doped with iron (III) and lanthanum for the degradation of organic pollutants," *Applied Surface Science*, vol. 257, no. 17, pp. 7671–7677, 2011.

[20] M. A. Barakat, G. Hayes, and S. I. Shah, "Effect of cobalt doping on the phase transformation of TiO_2 nanoparticles," *Journal of Nanoscience & Nanotechnology*, vol. 5, no. 5, pp. 759–765, 2005.

[21] T. Sun, J. Fan, E. Liu et al., "Fe and Ni co-doped TiO_2 nanoparticles prepared by alcohol-thermal method: application in hydrogen evolution by water splitting under visible light irradiation," *Powder Technology*, vol. 228, pp. 210–218, 2012.

[22] S. Iyyapushpam, S. T. Nishanthi, and D. Pathinettam Padiyan, "Photocatalytic degradation of methyl orange using α-Bi_2O_3 prepared without surfactant," *Journal of Alloys and Compounds*, vol. 563, pp. 104–107, 2013.

[23] G. Blanchard, M. Maunaye, and G. Martin, "Removal of heavy metals from waters by means of natural zeolites," *Water Research*, vol. 18, no. 12, pp. 1501–1507, 1984.

[24] Y. Wang, Y. He, T. Li, J. Cai, M. Luo, and L. Zhao, "Novel $CaBi_6O_{10}$ photocatalyst for methylene blue degradation under visible light irradiation," *Catalysis Communication*, vol. 18, pp. 161–164, 2012.

[25] R. Saravanan, S. Joicy, V. K. Gupta, V. Narayanan, and A. Stephen, "Visible light induced degradation of methylene blue using CeO_2/V_2O_5 and CeO_2/CuO catalysts," *Materials Science and Engineering C*, vol. 33, no. 8, pp. 4725–4731, 2013.

[26] R. Saravanan, H. Shankar, T. Prakash, V. Narayanan, and A. Stephen, "ZnO/CdO composite nanorods for photocatalytic degradation of methylene blue under visible light," *Materials Chemistry and Physics*, vol. 125, no. 1-2, pp. 277–280, 2011.

[27] F. Jiang, T. Yan, H. Chen, A. Sun, C. Xu, and X. Wang, "A g-C_3N_4-CdS composite catalyst with high visible-light-driven catalytic activity and photostability for methylene blue degradation," *Applied Surface Science*, vol. 295, pp. 164–172, 2014.

[28] W. Yu, X. Liu, L. Pan et al., "Enhanced visible light photocatalytic degradation of methylene blue by F-doped TiO_2," *Applied Surface Science*, vol. 319, pp. 107–112, 2014.